Electrical Power and Energy Systems 99 (2018) 434–446

Contents lists available at ScienceDirect

Electrical Power and Energy Systems

journal homepage: www.elsevier.com/locate/ijepes

Dynamic performance analysis, stability margin improvement and transfer power capability enhancement in DFIG based wind turbines at weak ac grid conditions

Amir Hosein Azizi, Mohsen Rahimi*

Department of Electrical and Computer Engineering, University of Kashan, Kashan, Iran

ARTICLE INFO

Keywords:
DFIG wind turbine
PLL dynamics
Weak grid connections
Grid short circuit ratio
Rotor virtual inductance

ABSTRACT

Wind farms are usually located in remote areas far away from utility grid and load centers. Hence, long transmission lines, used between wind farms and utility grid, result in a low value for the grid strength at connection point. This paper first studies stability of the grid connected DFIG wind turbine taking the PLL dynamics into account, and then presents an efficient control approach to stabilize the system and to enhance transfer power capability at weak grid conditions. Hence, unified dynamic modeling of the whole DFIG, including dynamics of the PLL, stator flux, rotor current, drive train, dc-link, rotor side converter (RSC) and grid side converter (GSC) current controllers, dc-link voltage and generator speed controllers, and grid is presented. Then, small signal stability of the full system is carried out and impact of the grid short circuit ratio (SCR) on stability of the system is examined. Next, rotor control structure is modified to increase the stability margin and transfer power capability under weak grid conditions. By the modified control structure, the grid SCR is virtually increased to enhance the system performance at weak grid connections. Finally, results of theoretical analyses are verified by time domain simulations conducted in MATLAB-Simulink environment.

1. Introduction

In the development of wind turbine (WT) technology, several types of WTs such as fixed speed type, limited variable speed WT, doubly-fed induction generator (DFIG), and full-scale variable speed WT have been considered [1,2]. Among the different alternatives to obtain variable speed, the system based on DFIG-WT has become the most popular [3]. As shown in Fig. 1, the DFIG stator winding is directly connected to the grid, and the rotor winding is supplied from the back-to-back voltage source converters (VSCs), known as rotor side converter (RSC) and grid side converter (GSC).

In this paper, the RSC is used for the generator speed control, and reactive power support, and the GSC for the dc-link voltage control and reactive power regulation [4]. The grid synchronization is a main step for the control of the RSC and GSC that is normally done by using the phase locked loop (PLL). This paper first examines stability of the grid connected DFIG wind turbine system taking the PLL dynamics into account, and then proposes a new control approach to stabilize the system under weak ac grid conditions.

Wind farms are usually placed in remote areas far away from the utility grid and consumer centers. Hence, long transmission lines should be used between the wind farms and utility grid that result in the grid strength to be weak. The strength of the electrical grid is usually determined by the value of the grid short circuit ratio (SCR), where the grid SCR is defined as the grid short circuit power at the connection point (point A in Fig. 1) to the wind turbine rated power. Hence, the higher value of the grid SCR means the more strength for the grid.

At present, some papers [5–13] have dealt with the modeling, control and stability analysis of the grid connected VSCs, in full converter wind turbines and VSC HVDC systems, by taking the PLL dynamics into account, under weak grid conditions. However, these references are not related to DFIG based WTs, and does not propose modified control approach for improving the DFIG performance and enhancing transfer power capability at weak grid connections. Ref. [6] deals with the modeling and control of VSC-HVDC system connected to weak ac system. The Refs. [5,7,8] study the impact of the PLL on the stability of the grid connected VSC at weak ac grid conditions. In [12] performance of dc-link voltage control in full converter based wind turbine connected to weak grid is investigated, and the effects of grid strength, operating point, and control loops' interactions on dc-link voltage control dynamics are examined. Also, Ref. [13] deals with the stability analysis of the full converter based WT during deep voltage

* Corresponding author.
E-mail address: mrahimi@kashanu.ac.ir (M. Rahimi).

https://doi.org/10.1016/j.ijepes.2018.01.040
Received 22 October 2017; Received in revised form 22 January 2018; Accepted 23 January 2018

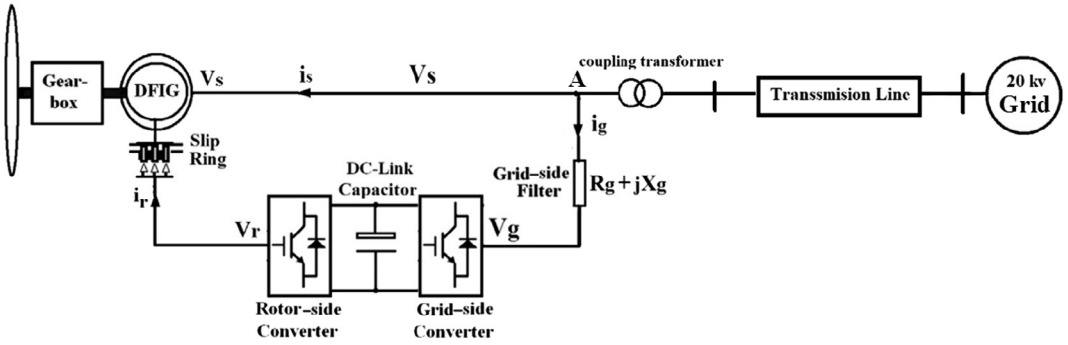

Fig. 1. Grid connected DFIG based WT.

sag, when the WT connected to a high-impedance ac grid. It develops the WT dynamic model that reflects the interaction between the PLL and alternating current control, and then modal analysis is conducted to extract the unstable modes.

Dynamic performance evaluation and stability analysis of the DFIG based WTs have been reported in several research papers [14–19]. However, little analytical work has been published regarding the DFIG stability analysis under weak grid conditions taking the PLL dynamics into account. In [20,21], the stability of the dc-link voltage in a DFIG based WT, connected to a weak ac grid, is studied by considering the PLL dynamics. Ref. [22] develops a reduced order small signal model to examine the dc link voltage stability in DFIG based WT, under weak ac grid conditions. It investigates the effects of operating points, grid strengths and control loops interactions on the DFIG dynamic performance.

Even though, dynamic stability of the DFIG connected to weak ac grid has been studied in some papers, such as [18–20], however, to the best knowledge of the authors, less analytical work has dealt with the improvement of the DFIG stability under weak ac grid conditions.

In [23,24] active compensators are presented for improvement of ride through capability and transient behavior in DFIG based WTs. These approaches, modify the rotor current reference by adding auxiliary damping signals obtained by the feedback of the stator flux and rotor current. However, the control approaches, working based on the stator flux feedback, only increase the damping of the stator flux and transient response during the voltage dip, and enhance the LVRT capability. Also, some papers, such as [25–30], use flexible ac transmission systems (FACTS) and energy storages devices for improving the transfer power capability and system stability in grid connected DFIG based wind turbines. However, these approaches, using active hardware such as FACTS controllers, energy storages, and power electronic devices, are costly.

In this way, the main contributions of the paper are as follows: (a) Extracting the stator and grid dynamics, and small signal stability analysis of the DFIG system taking the PLL dynamics into account. (b) Proposing a new active compensator, by modifying the rotor side converter control structure, to improve the stability margin, and to enhance the transfer power capability at weak ac grid conditions.

The outlines of the paper are given as follows. This paper indeed deals with the stability analysis and dynamic performance enhancement of the grid connected DFIG based WTs under weak ac grid conditions. In this way, detailed dynamic modeling of the whole DFIG system, including the dynamics of the PLL, stator flux, rotor current, drive train, dc-link, RSC and GSC current controllers, dc-link voltage and generator speed controllers, and grid, is presented. Then, based on the linearized model of the entire DFIG system, small signal stability of the full system is conducted and impact of the grid SCR on the stability of the system is examined. Next, the RSC control structure is modified to increase the stability margin of the DFIG system under weak ac grid conditions. The modified control structure introduces negative virtual inductance at the stator side, and virtually increases the grid SCR to stabilize the system at weak grid connections. At the end, results of theoretical analyses are verified by time domain simulations.

2. DFIG synchronization and PLL dynamics

Phase-locked loop (PLL) is one of the basic building blocks used in grid connected DFIG-based wind turbines for grid synchronization. The synchronous reference frame PLL (SRF-PLL) is the most popular type of the PLL widely used in three-phase applications [31,32]. In this paper, the RSC and GSC are controlled in dq-frame with the stator voltage orientation (SVO), in which the d-axis is aligned with the vector of the stator voltage .To do this, an SRF-PLL is implemented to extract the phase and frequency of the stator voltage. Fig. 2 depicts the structure of the SRF-PLL, in which, first the three-phase stator voltages v_{sabc} are transformed into the stationary frame ($\alpha\beta$ - frame) and then $v_{s\alpha\beta}$ are transformed to the rotating dq reference frame using the argument θ_{pll}, where θ_{pll} is the phase angle extracted by the PLL. The phase angle θ_{pll} is obtained by using a PI-controller ($K_{PLL}(s)$) in a feedback loop that forces the q-component of the stator voltage to zero, i.e. $v_{sq} = 0$ and $v_{sd} = V_s$. In Fig. 2, the three phase stator voltages v_{sabc} are in per unit (pu).

According to Fig. 2 and considering the PI controller of the PLL loop as $K_{PLL}(s) = k_{p-pll} + \frac{k_{i-pll}}{s}$, the linearized state equations of the PLL are given by

$$\frac{d\Delta x_{pll}}{dt} = \Delta v_{sq} \tag{1}$$

$$\Delta\omega_{pll} = k_{p-pll}\Delta v_{qs} + k_{i-pll}\Delta x_{pll} \tag{2}$$

$$\frac{d\Delta\theta_{pll}}{dt} = \omega_b.\ \Delta\omega_{pll} \tag{3}$$

where the symbol Δ denotes the small deviation around the operating point, and x_{pll} represents the state variable corresponding to PI controller of Fig. 2.

For the balanced three-phase stator voltages with $v_{as}(t) = V_s\cos\theta_g(t)$, we have

$$v_{\alpha\beta s} = \frac{2}{3}[v_{as}(t) + e^{j120}v_{bs}(t) + e^{-j120}v_{cs}(t)] = V_s e^{j\theta_g} \tag{4}$$

Using (4), v_{sd} and v_{sq}, in Fig. 2, are obtained as

$$v_{sd} = V_s\cos(\theta_g - \theta_{pll}) \tag{5}$$

$$v_{sq} = V_s\sin(\theta_g - \theta_{pll})$$

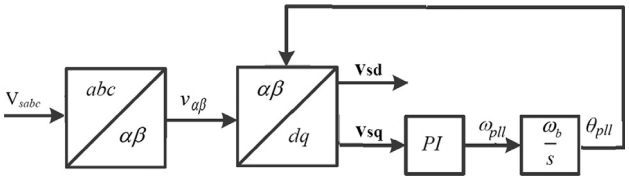

Fig. 2. Block diagram of the SRF-PLL.

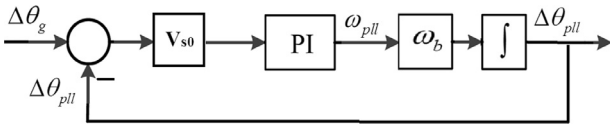

Fig. 3. Linearized control loop of the PLL.

By linearizing (5) around the operating point, i.e. θ_{pll_0} and θ_{g_0} where $\theta_{g_0} = \theta_{pll_0}$, we have

$$\Delta v_{sd} = \Delta V_s$$
$$\Delta v_{sq} = V_{s_0}(\Delta\theta_g - \Delta\theta_{pll}) \tag{6}$$

where the symbol Δ denotes the small signal value and the subscript 0 denotes the operating point. According to (6) and Fig. 2, the PLL linearized control loop, used for estimation of the phase and frequency of the stator voltage, is obtained as depicted in Fig. 3.

Where V_{s0} in Fig. 3 is the stator voltage amplitude at operating point and is equal to 1 pu. Considering Fig. 3, the transfer function from $\Delta\theta_g$ to $\Delta\theta_{pll}$ is obtained as

$$T_{s-pll}(s) = \frac{\Delta\theta_{pll}(s)}{\Delta\theta_g(s)} = \frac{k_{p-pll}ks + k_{i-pll}k}{s^2 + k_{p-pll}ks + k_{i-pll}k} \tag{7}$$

where k in (7) is $k = V_{s0}\omega_b$. By comparing $T_{s-pll}(s)$ with the general form of the second order transfer function, it is expressed that $\omega_n^2 = k_{i-pll}k$ and $2\xi\omega_n = k_{p-pll}k$ where by selecting $\omega_n = 20Hz$ and $\xi = 0.7$, the proportional and integral gains of the PLL controller are obtained.

3. Modeling of the stator and rotor dynamics in DFIG based WT

In this section, the dynamic model of the DFIG based wind turbine in the *dq* synchronous reference frame with the stator voltage orientation (SVO) is presented. In this way, the positive direction for the rotor and stator currents are considered into the windings and all system parameters and variables are given in per unit (pu). It is noted that, for the control of the DFIG in the SVO frame, we have indeed two dq frames: (1) PLL dq frame in which the angle θ_{PLL} estimated by the PLL is used for doing the dq transformation, (2) Ideal dq frame in which the angle θ_g is used to perform the dq transformation and the d-axis is always perfectly aligned with the stator voltage vector. In steady state conditions, $\theta_{PLL} = \theta_g$ and both the PLL and ideal dq frames are identical, however, this may not be necessarily true during transient conditions. In actual conditions, we do not directly access to θ_g, and thus we use θ_{PLL}, as the estimated value of θ_g, for the dq transformation. In other words, in actual conditions, we indeed transform the machine equations into the PLL reference frame for the system analysis and controller design.

The basic equations of the stator and rotor voltages and fluxes, and electromagnetic torque in the dq reference frame rotating at angular speed of ω_{pll} are given by [33]:

$$v_{sdq} = R_s i_{sdq} + j\omega_{pll}\psi_{sdq} + \frac{1}{\omega_b}\frac{d\psi_{sdq}}{dt} \tag{8}$$

$$v_{rdq} = R_r i_{rdq} + j\omega_2\psi_{rdq} + \frac{1}{\omega_b}\frac{d\psi_{rdq}}{dt} \tag{9}$$

$$\psi_{sdq} = L_s i_{sdq} + L_m i_{rdq} \tag{10}$$

$$\psi_{rdq} = L_m i_{sdq} + L_r i_{rdq} \tag{11}$$

$$T_e = \frac{L_m}{L_s}(\psi_{sq} i_{rd} - \psi_{sd} i_{rq}) \tag{12}$$

where the subscripts s and r denote the stator and rotor quantities, v, i and ψ denote the voltage, current and flux, ω_2 is the rotor slip frequency, ω_b is the base angular frequency, L_s and L_r are the stator and rotor self-inductances, and L_m is the machine magnetizing inductance. ω_{pll} is the frequency of the stator voltage extracted by the PLL and is indeed the rotational speed of the dq axes in the SVO frame. In the SVO frame, the d-axis of the frame is aligned with the stator voltage vector, and thus at steady state conditions, $v_{sd} = |V_s|$ and $v_{sq} = 0$, where $|V_s|$ is the stator voltage amplitude. By neglecting the stator resistance, the dq stator voltages at steady state conditions can be given as $v_{sd} \cong -\omega_s\psi_{sq}$ and $v_{sq} \cong \omega_s\psi_{sd}$, where $\omega_{pll} = \omega_s$ and $\omega_s = 1$ pu. This means that at the dq reference frame with SVO, the steady state values of the dq components of the stator flux are $\psi_{sd} \cong 0$ and $\psi_{sq} \cong -|\psi_s|$. Considering (12) and according to the explanations given above, the electromagnetic torque in the SVO frame can be given as $T_e = \frac{L_m}{L_s}(\psi_{sq} i_{rd}) \approx -\frac{L_m}{L_s}(|\psi_s| i_{rd})$. Hence, in the SVO frame, the electromagnetic torque and consequently the generator speed can be controlled by the d-axis component of the rotor current, i_{rd}. Also, the reactive power injected to the grid by the stator, as a function of the rotor current in the SVO frame, is given by $Q_s = -\frac{|V_s|^2}{X_s} - \frac{L_m}{L_s}|V_s| i_{rq}$, and thus the stator reactive power can be controlled by the q-axis rotor current, i_{rq}.

3.1. Stator and grid modeling

In Fig. 1, the DFIG is connected to the grid, where from the stator side, the WT transformer, the grid and transmission line can be modeled with the Thevenin representation comprising the infinite bus e_∞ in series with the resistance R_e and inductance L_e (see Fig. 4). Considering Fig. 4, the linearized form of the grid dynamics can be described by the following equation as a function of the stator flux and current and GSC current.

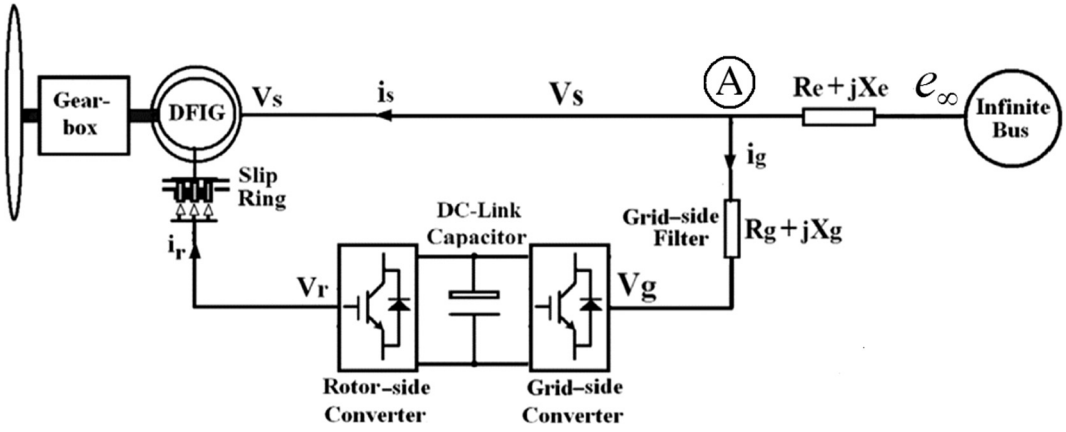

Fig. 4. Simplified form of the grid connected DFIG based WT.

$$\Delta v_{sdq} = -\frac{R_e}{L_s}\Delta\psi_{sdq} + \frac{R_e L_m}{L_s}\Delta i_{rdq} - R_e \Delta i_{gdq} - \frac{L_e}{\omega_b L_s}\frac{d\Delta\psi_{sdq}}{dt} + \frac{L_e L_m}{\omega_b L_s}\frac{d\Delta i_{rdq}}{dt} - \frac{L_e}{\omega_b}\frac{d\Delta i_{gdq}}{dt} - j\frac{L_e \Delta\omega_{pll}}{L_s}\psi_{sdq0} - j\frac{L_e \omega_{pll0}}{L_s}\Delta\psi_{sdq} + j\frac{L_e L_m \Delta\omega_{pll}}{L_s} i_{rdq} + j\frac{L_e L_m \omega_{pll0}}{L_s}\Delta i_{rdq} - jL_e L_m \Delta\omega_{PLL} i_{gdq} - jL_e L_m \omega_{pll0}\Delta i_{gdq} + \Delta e_{\infty dq} \quad (13)$$

where the symbol Δ denotes the small variation around the operating point, and the subscript 0 represents the operating point.

From (8), (10) and (11), the linearized form of the dq stator fluxes can be expressed by the following state equations:

$$\frac{1}{\omega_b}\frac{d\Delta\psi_{sdq}}{dt} = -\frac{R_s}{L_s}\Delta\psi_{sdq} + \frac{R_s}{L_s}L_m \Delta i_{rdq} - j\omega_{pll_0}\Delta\psi_{sdq} - j\psi_{sdq_0}\Delta\omega_{pll} + \Delta v_{sdq} \quad (14)$$

Assuming the phase a of the infinite bus voltage is $e_{a\infty}(t) = E\cos\theta_e$, the dq components of the infinite bus voltage in the SVO frame are

$$e_{\infty d} = E\cos(\theta_e - \theta_{pll})$$
$$e_{\infty d} = E\sin(\theta_e - \theta_{pll}) \quad (15)$$

where θ_{pll} is the phase of the stator voltage extracted by the PLL. From (15), the linearized forms of the $e_{\infty d}$ and $e_{\infty q}$ are obtained as

$$\Delta e_{\infty d} = E\sin\gamma_0(\Delta\theta_e - \Delta\theta_{pll})$$
$$\Delta e_{\infty q} = E\cos\gamma_0(\Delta\theta_e - \Delta\theta_{pll}) \quad (16)$$

where $\gamma_0 = \theta_{pll_0} - \theta_{e_0}$. Considering Fig. 4 and neglecting R_e, the phasor diagram of the stator voltage and grid current at steady state and unity power factor operation is obtained as depicted in Fig. 5.

Considering Figs. 4 and 5, the active power injected to the grid by the DFIG is given by

$$P_g = \frac{E|V_{s0}|}{X_e}\sin\gamma_0 \quad (17)$$

Hence, according to Fig. 5 and (17), $E\cos\gamma_0$ in (16) is equal to $V_{s_0} = 1\,pu$, and $E\sin\gamma_0$ is equal to $\frac{P_g X_e}{|V_{S0}|}$.

3.2. Modeling of rotor and corresponding controllers

From (8)-(11), the rotor dynamics is described, in terms of rotor current and stator flux, as follows [22]:

$$v_{rdq} = R_r' i_{rdq} + j\omega_2 L_r' i_{rdq} + \frac{L_r'}{\omega_b}\frac{di_{rdq}}{dt} + e_{rdq} \quad (18)$$

where, $R_r' = R_r + R_s(L_m/L_s)^2$ is the transient resistance, $L_r' = L_r - (L_m/L_s)^2$, is the transient inductance of the rotor current

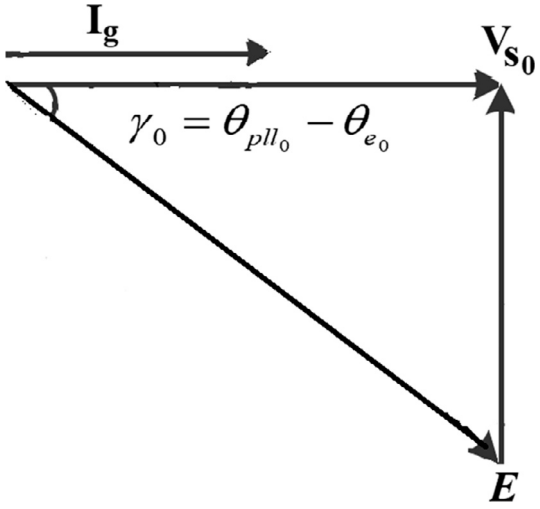

Fig. 5. Phasor diagram of the stator voltage and grid current at unity power factor operation.

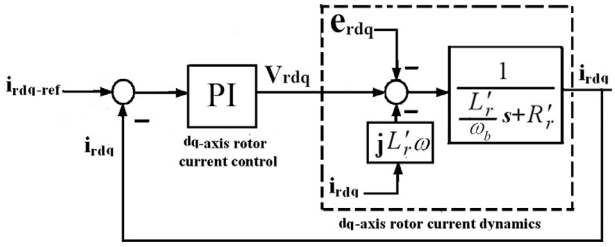

Fig. 6. Rotor dq-axes current control loops.

dynamics, L_s and L_r are the stator and rotor self-inductances, and L_m is the machine magnetizing inductance.

Also, e_{rdq} in (21) is the rotor back-emf voltages depending on the stator voltage and flux, and is given by $e_{rdq} = \frac{L_m}{L_s}\left(V_{sdq} - \frac{R_s}{L_s}\psi_{sdq} - j\omega_r\psi_{sdq}\right)$. Fig. 6 shows the rotor dq current control loop, considering the rotor controller to be PI, i.e. $K_{ir}(s) = k_{p-i_r} + \frac{k_{i-i_r}}{s}$. The output of the rotor current controller determine the rotor dq voltage that should be generated by the RSC.

According to Fig. 6, the linearized dynamics of the rotor current is given by

$$\frac{L_r'}{\omega_b}\frac{d\Delta i_{rdq}}{dt} = -R_r'\Delta i_{rdq} - \Delta e_{rdq} - jL_r' i_{rdq0}\Delta\omega_2 - jL_r'\omega_{20}\Delta i_{rdq} + k_{p-i_r}(\Delta i_{rdq-ref} - \Delta i_{rdq}) + \Delta x_{irdq} \quad (19)$$

where x_{irdq} is the state variable corresponding to rotor current controller, and is described by

$$\frac{d\Delta x_{irdq}}{dt} = k_{i-i_r}(\Delta i_{rdq-ref} - \Delta i_{rdq}) \quad (20)$$

3.3. Speed and reactive power controller

In the dynamic studies of DFIG, the two mass model is used for modeling the drive train system, where the linearized two mass drive train model is given as follows [34]:

$$2H_r\frac{d\Delta\omega_r}{dt} = \Delta T_e + \Delta T_{sh}$$
$$\frac{d\Delta\theta}{dt} = \omega_b(\Delta\omega_t - \Delta\omega_r)$$
$$2H_t\frac{d\Delta\omega_t}{dt} = \Delta T_m - \Delta T_{sh}$$
$$\Delta T_{sh} = K_{cs}\Delta\theta + D_c(\Delta\omega_t - \Delta\omega_r) \quad (21)$$

where T_m and T_e are the turbine and generator electrical torque in pu, respectively, T_{sh} is the shaft torsional torque in pu, ω_t and ω_r are the turbine and generator rotational speeds in pu, θ is the shaft twist angle in rad, H_t and H_r are the inertia constants of the turbine and generator in sec, respectively, k_{cs} is the shaft stiffness coefficient in pu/elec. rad, D_c is the damping coefficient in pu.

In the frame with SVO, the d-axis components of the rotor voltage and current, v_{rd} and i_{rd}, can be used for the control of the rotor speed. Fig. 7 shows the generator speed control loop, in which the term $\frac{\alpha_{rdq}}{s+\alpha_{rdq}}$ is the closed loop transfer function of the inner rotor current control loop. The reference speed ω_{r-ref} is obtained based on the predefined power speed curve provided by the wind turbine manufacture.

Considering the speed controller to be PI, $K_\omega(s) = k_{p-\omega} + \frac{k_{i-\omega}}{s}$, the linearized state equation of the speed controller is given by

$$\frac{d\Delta x_\omega}{dt} = k_{i-\omega}(\Delta\omega_{r-ref} - \Delta\omega_r) \quad (22)$$

From Fig. 7, the linearized from of the d-axis rotor reference current is given by:

$$\Delta i_{rd-ref} = -k_{p-\omega}(\Delta\omega_{r-ref} - \Delta\omega_r) - \Delta x_\omega \quad (23)$$

In the SVO frame, the reactive power injected to the gird by the

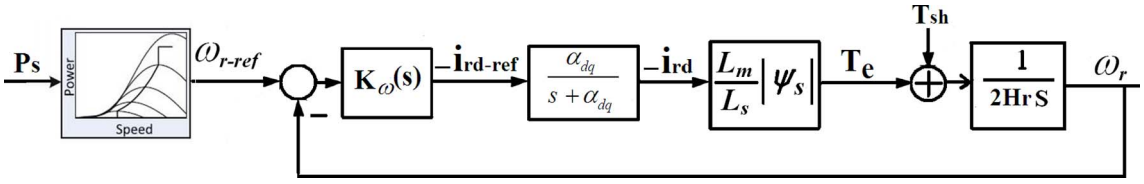

Fig. 7. Wind turbine speed control loop.

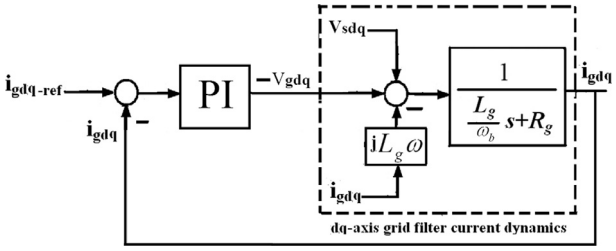

Fig. 8. Grid-side converter (GSC) current loop.

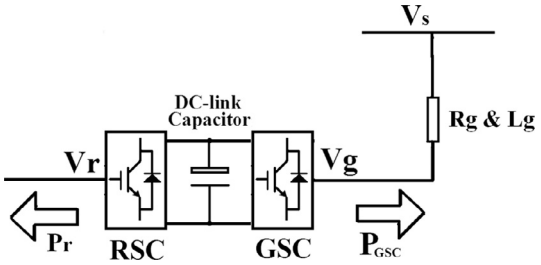

Fig. 9. Active power flow in RSC and GSC.

stator can be controlled by the q-axis axis rotor current i_{rq}. The control loop related to stator reactive power control is given in [14].

Considering the reactive power controller as $K_Q(s) = k_{p_Q} + \frac{k_{i_Q}}{s}$, the state equation related to reactive power controller is given by:

$$\frac{d\Delta x_Q}{dt} = k_{iQ}(\Delta Q_{s-ref} - \Delta Q_s) \tag{24}$$

Also, the rotor q-axis reference current is given by

$$\Delta i_{rq-ref} = k_{pQ}(\Delta Q_{s-ref} - \Delta Q_s) + \Delta x_Q \tag{25}$$

3.4. Modeling of the GSC and DC link capacitor

As shown in Fig. 4, the GSC is connected to the grid via interfaced filter modeled with inductance L_g and resistance R_g. The dynamics of the GSC and corresponding interfaced filter in the PLL reference frame is given by

$$v_s - v_g = R_g i_g + jL_g\omega_{pll} i_g + \frac{L_g}{\omega_b}\frac{di_g}{dt} \tag{26}$$

Fig. 8 shows the dq GSC current control loop considering the current controller to be PI, i.e. $K_{G_{dq}}(s) = k_{p-i_g} + \frac{k_{i-i_g}}{s}$.

Considering Fig. 8, the linearized GSC current dynamics can be presented as

Table 1
System modes and dominant state variables for SCR = 5.

Modes	Modes for SCR = 5	Dominant state variable
$\lambda_{1,2}$	$-180.8 \pm j549.4$	i_{rd}, i_{rq}
$\lambda_{3,4}$	$-169.9 \pm j241.2$	i_{gd}, i_{gq}
$\boldsymbol{\lambda_{5,6}}$	$\boldsymbol{-6.85 \pm j162.8}$	$\boldsymbol{i_{rd}, V_{DC}}$
$\lambda_{7,8}$	$-75.6 \pm j78.04$	x_{pll}, θ_{pll}
$\lambda_{9,10}$	-76.58	x_{ird}, x_{dc}
$\lambda_{11,12}$	$-36.94 \pm j22.75$	x_{ird}, x_{irq}
$\lambda_{13,14}$	$-4.9 \pm j11.22$	ω_r, θ
λ_{15}	-4.33	x_Q
λ_{16}	-2.35	x_{igd}
$\lambda_{17,18}$	$-1.82 \pm j0.81$	ω_t, x_{igq}
λ_{19}	-0.64	x_ω

$$\frac{L_g}{\omega_b}\frac{d\Delta i_{gdq}}{dt} = -R_g\Delta i_{gdq} - jL_g\omega_{pll0}\Delta i_{gdq} - jL_g i_{gdq0}\Delta\omega_{pll} + k_{p-i_g}(\Delta i_{gdq-ref} - \Delta i_{gdq}) + \Delta x_{igdq} + \Delta v_{sdq}$$

$$\frac{d\Delta x_{igdq}}{dt} = k_{i-i_g}(\Delta i_{gdq-ref} - \Delta i_{gdq}) \tag{27}$$

The task of DC-link voltage controller is the power balancing between RSC and GSC. According to Fig. 9, and neglecting the converter losses, we have

$$CV_{dc}\frac{dV_{dc}}{dt} = S_b(P_{GSC} - P_r) \tag{28}$$

where S_b is the base value for the system power, and P_r and P_{GSC} are the rotor and GSC input powers and are given by $P_{GSC} = (v_{dg}i_{gd} + v_{gq}i_{gq})$ and $P_r = (v_{rd}i_{rd} + v_{rq}i_{rq})$. Fig. 10 shows the DC-link voltage control loop, where the DC-link voltage controller provides the d-axis reference current for the GSC inner current control loop.

Using a PI controller stated as $K_{dc}(s) = k_{p-dc} + \frac{k_{i-dc}}{s}$, the linearized state equation of the DC-link voltage controller is given by

$$\frac{d\Delta x_{dc}}{dt} = k_{i-dc}(\Delta V_{dc-ref} - \Delta V_{dc}) \tag{29}$$

4. Small signal stability analysis

The Eqs. (1)–(3), (6), (13), (14), (16), (19)–(25) and (27)–(29) describe the full dynamics of the DFIG based wind turbine, comprising the dynamics of PLL, stator, grid, rotor, drive train, GSC, dc link capacitor, and system controllers. Linearizing the above mentioned equations, the full DFIG system can be described as

$$\dot{\Delta x} = A\Delta x + B\Delta u \tag{30}$$

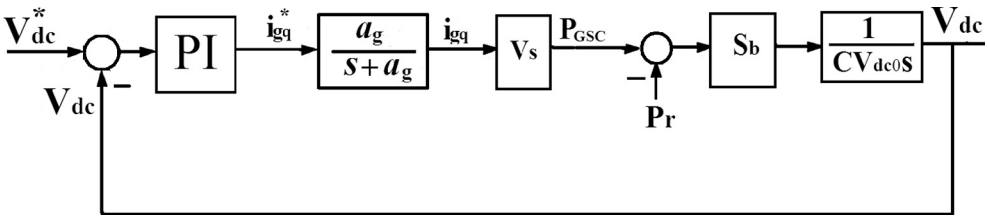

Fig. 10. DC-link voltage control loop.

Table 2
System modes for different values of the grid SCR, i.e. SCR = 3–6.

Modes	Modes for SCR = 3	Dominant state variable	Modes for SCR = 4	Modes for SCR = 5	Modes for SCR = 6
$\lambda_{1,2}$	$-168.2 \pm j590.2$	i_{rd},i_{rq}	$-178.6 \pm j571.7$	$-180.8 \pm j549.4$	$-181.6 \pm j530.5$
$\lambda_{3,4}$	$-1.74 \pm j1.25$	i_{gd},i_{gq}	$-168.1 \pm j239.4$	$-169.9 \pm j241.2$	$-174.8 \pm j240.4$
$\boldsymbol{\lambda_{5,6}}$	$\mathbf{1.46 \pm j125.5}$	$\boldsymbol{i_{rd}}$,$\boldsymbol{V_{DC}}$	$\mathbf{-2.20 \pm j154.4}$	$\mathbf{-6.85 \pm j162.8}$	$\mathbf{-11.1 \pm j169.9}$
$\lambda_{7,8}$	$-64.3 \pm j80.3$	x_{pll},θ_{pll}	$-72.9 \pm j79.14$	$-75.6 \pm j78.04$	$-76.8 \pm j76.7$
$\lambda_{9,10}$	$-75.05 \pm j37.8$	x_{ird},x_{dc}	$-92.32 \pm j19.68$	-76.58	-70
$\lambda_{11,12}$	$-27.02 \pm j20.6$	x_{ird},x_{irq}	$-33.58 \pm j22.94$	$-36.94 \pm j22.75$	$-39.9 \pm j22.11$
$\lambda_{13,14}$	$-4.18 \pm j12.5$	ω_r,θ	$-4.84 \pm j11.47$	$-4.9 \pm j11.22$	$-5.01 \pm j11.04$
λ_{15}	-4.30	x_Q	-4.36	-4.33	-4.30
λ_{16}	-3.7	x_{igd}	-2.35	-2.35	-2.35
$\lambda_{17,18}$	$-1.74 \pm j1.25$	ω_t,x_{igq}	$-1.75 \pm j0.87$	$-1.82 \pm j0.81$	$-1.87 \pm j0.75$
λ_{19}	-0.53	x_ω	-0.63	-0.64	-0.64

Table 3
Modal analysis for the case with rotor virtual inductance, and for SCR = 3 and 4.

		Modes after implementation	Dominant state variable		Modes for SCR = 4
Short circuit ratio (SCR) = 3	$\lambda_{1,2}$	$-182.3 \pm j619.7$	i_{rd},i_{rq}	Short circuit ratio = 4	$-178.6 \pm j571.7$
	$\lambda_{3,4}$	$-154.3 \pm j228.4$	i_{gd},i_{gq}		$-168.1 \pm j239.4$
	$\boldsymbol{\lambda_{5,6}}$	$\mathbf{-2.08 \pm j151.71}$	$\boldsymbol{i_{rd}}$,$\boldsymbol{V_{DC}}$		$\mathbf{-2.20 \pm j154.4}$
	$\lambda_{7,8}$	$-76.63 \pm j79.84$	x_{pll},θ_{pll}		$-72.9 \pm j79.14$
	$\lambda_{9,10}$	$-47.75 \pm j37.43$	x_{ird},x_{dc}		$-92.32 \pm j19.68$
	$\lambda_{11,12}$	$-39.8 \pm j24.54$	x_{ird},x_{irq}		$-33.58 \pm j22.94$
	$\lambda_{13,14}$	$-4.54 \pm j12.07$	ω_r,θ		$-4.84 \pm j11.47$
	λ_{15}	-4.32	x_Q		-4.36
	λ_{16}	-2.35	x_{igd}		-2.35
	$\lambda_{17,18}$	$-1.65 \pm j0.95$	ω_t,x_{igq}		$-1.75 \pm j0.87$
	λ_{19}	-0.98	x_ω		-0.63

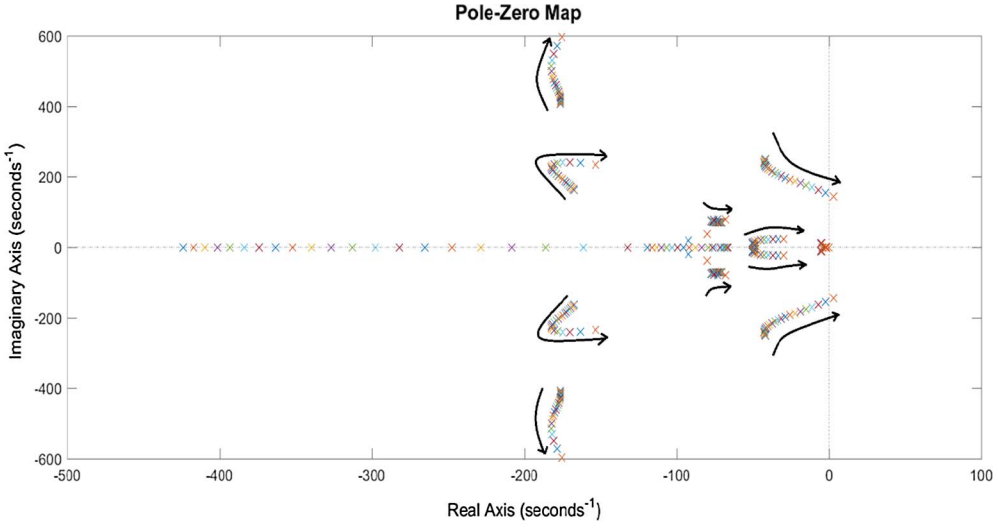

Fig. 11. Eigenvalue value Locus for the modes $\lambda_{5,6}$ and under varying the SCR from 20 to 3.

where A is the 19×19 state matrix, and x and u are the vectors of state variables, and exogenous inputs, and $\boldsymbol{x} = [\theta_{pll},x_{pll},\psi_{sd},\psi_{sq},i_{rd},i_{rq},x_{ird},x_{irq},\omega_r,\theta,\omega_t,x_\omega,x_Q,i_{gd},i_{gq},x_{igd},x_{igq},V_{DC},x_{dc}]^T$, $u = [E,V_w,Q_{s-ref},V_{dc-ref}]^T$.

Modal analysis is done on the study system of Fig. 4 with parameters of Appendix A. The operating conditions correspond to wind speed of 11 m/s and unity power factor at the stator and GSC terminals. The PI controllers parameters correspond to the rotor and grid-side filter current control bandwidths of 2 per unit (628 rad/s), speed control loop bandwidth of 4.4 rad/s (0.7 Hz), reactive power control loop bandwidth of 4.4 rad/s (0.7 Hz), PLL control bandwidth of 25 Hz, and dc link voltage control bandwidth of 25 Hz. Table 1 shows the system modes and dominant state variables related to each mode for the grid short circuit ratio (SCR) equal to 5. By using the participation factors [35], the degree of contribution of each state variable in the system modes, and the consequently the dominant state variables are obtained (see Appendix B). Considering Fig. 4, the SCR is defined as the grid short circuit power at point A to the WT rated power.

According to Table 1, the following findings are given: (1) The modes $\lambda_{1,2} = -180.8 \pm j549.4$ are the dq rotor current modes, and i_{rd} and i_{rq} have the most contribution in them. (2) The modes $\lambda_{3,4} = -169.9 \pm j241.2$ are the GSC current modes associated with state variables i_{gd} and i_{gq}. (3) The modes $\lambda_{5,6} = -6.85 \pm j162.8$ correspond to the state variables i_{rd} and V_{DC}. (4) The modes $\lambda_{7,8} = -75.6 \pm j78.04$ are the phase-locked loop modes, and x_{pll} and θ_{pll} have the most participation in these modes. (5) The modes $\lambda_{9,10} = -76.58$ are the rotor and

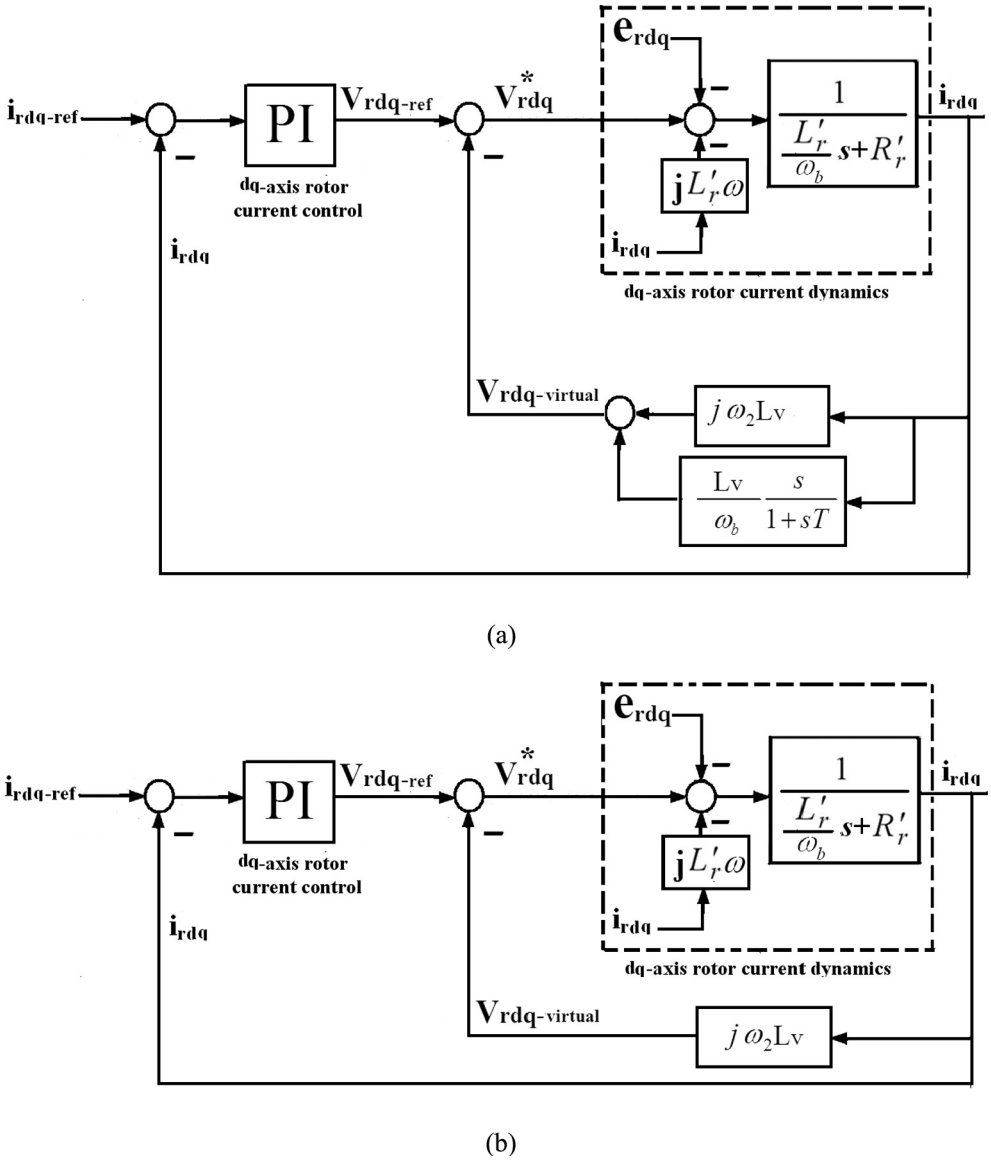

Fig. 12. Modified RSC current control to create the low frequency virtual inductance, (a) detailed representation, (b) simplified representation under quasi-steady state conditions.

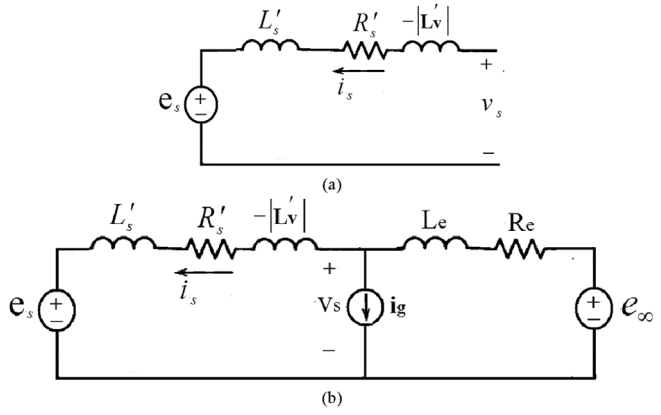

Fig. 13. (a) Equivalent circuit of the stator dynamics at quasi steady state conditions, (b) Quasi steady state equivalent circuit of the grid connected DFIG from the stator side point of view.

DC-link electrical modes associated with state variables x_{ird} and x_{dc} (see (20) and (29)). (6) The modes $\lambda_{11,12} = -36.94 \pm j22.75$ are associated with the rotor current controllers, i.e. state variables x_{ird} and x_{irq} (see (20)). (7) The modes $\lambda_{13,14} = -4.9 \pm j11.2$ are the electromechanical modes corresponding to state variables ω_r and shaft twist angle θ. (8) The real modes $\lambda_{15} = -4.33$ and $\lambda_{16} = -2.35$ correspond to state variables x_Q and x_{igd}, respectively. (9) The modes $\lambda_{17,18} = -1.82 \pm j0.81$ correspond to state variables ω_t and x_{igq}. (10) The real mode $\lambda_{19} = -0.64$ is related to the speed controller and the state variable x_ω has the most contribution in this mode.

Modal analysis shows that the grid SCR has an important role on the stability of the modes $\lambda_{5,6}$, and consequently on the stability of the whole system. Table 2 depicts the system modes for different values of grid SCR, SCR = 3–6. According to Table 2, by decreasing the grid SCR, the damping of the modes $\lambda_{5,6}$ decreases and for SCR = 3, the modes $\lambda_{5,6}$ and consequently the whole system become unstable.

Hence, the bold row in Tables 1–3 corresponds to the critical modes $\lambda_{5,6}$.

Fig. 11 shows the root locus graph of the modes $\lambda_{5,6}$ under gradual change of the SCR from 20 to 3. According to Fig. 11, the modes $\lambda_{5,6}$ move toward the right hand side of the s-plane, as the SCR decreases from 20 to 3, which indicates unstable conditions due to weak grid conditions.

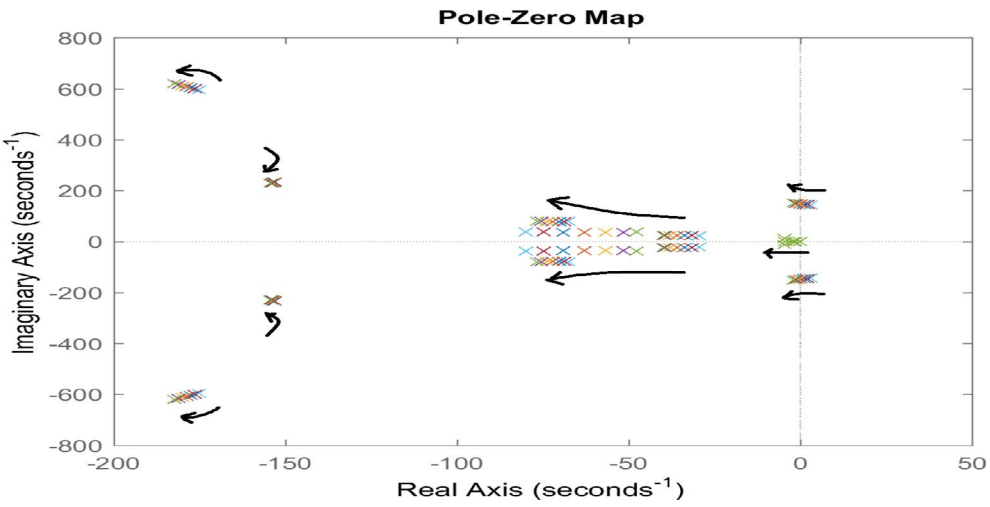

Fig. 14. Root locus graph of the modes $\lambda_{5,6}$ at SCR = 3, and for gradual change of the $|L_v|$ from 0 to 1 pu.

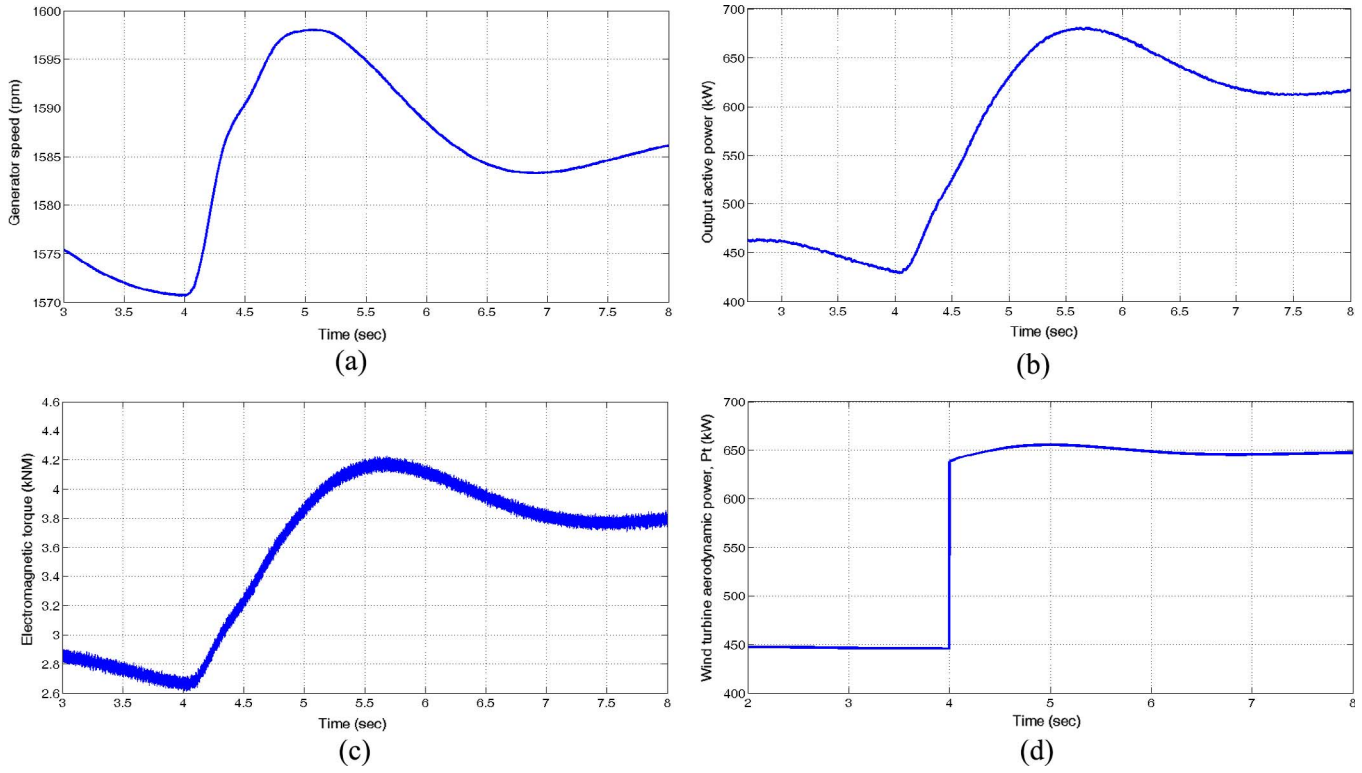

Fig. 15. Wind turbine responses to a step change of wind speed from 10 to 12 m/s at SCR = 5, (a) generator speed, (b) output active power injected to the grid, (c) electromagnetic torque, (d) wind turbine captured power.

5. RSC control modification and virtual impedance emulation

As stated in Section 4, by decreasing the grid SCR, the modes associated to the dc-link system move toward the unstable state, and for critical value of SCR = 3, the DFIG system becomes unstable. In this section, for stabilizing the DFIG system under weak grid conditions, the RSC control is modified to create a low frequency negative virtual inductance. This negative virtual inductance can enhance the stability margin and increase the steady state power transfer capability. Fig. 12(a) shows the modified RSC current control to create the low frequency virtual inductance.

In Fig. 12(a), the rotor reference currents are obtained from the outer speed and reactive power control loops, and the negative virtual inductance is realized by subtracting the virtual voltage $v_{rdq-virtual}$ from the controller output $v_{rdq-ref}$. Hence, the voltage produced by the RSC v^*_{rdq}, is given by

$$v^*_{rdq} = v_{rdq-ref} - v_{rdq-virtual}$$
$$v_{rdq-virtual} = j\omega_2 L_v i_{idq} + L_v \frac{i_{rdq}}{dt} \quad (31)$$

where, in (31) $L_v < 0$, and thus $L_v = -|L_v|$.

Under quasi-steady state conditions, $\frac{di_{rdq}}{dt}$ can be approximated with zero, and thus the modified control system can be simplified as depicted in Fig. 12(b). According to Fig. 12(b), under quasi-steady state conditions with $di_{rdq}/dt = 0$, we have

$$v_{rdq-ref} = R'_r i_{rdq} + j\omega_2 (L'_r - |L_v|) i_{rdq} + e_{rdq} \quad (32)$$

Also, from (8), the stator voltage at the quasi-steady state conditions can be given as

$$v_{sdq} = R_s i_{sdq} + j\omega_s \psi_{sq} \quad (33)$$

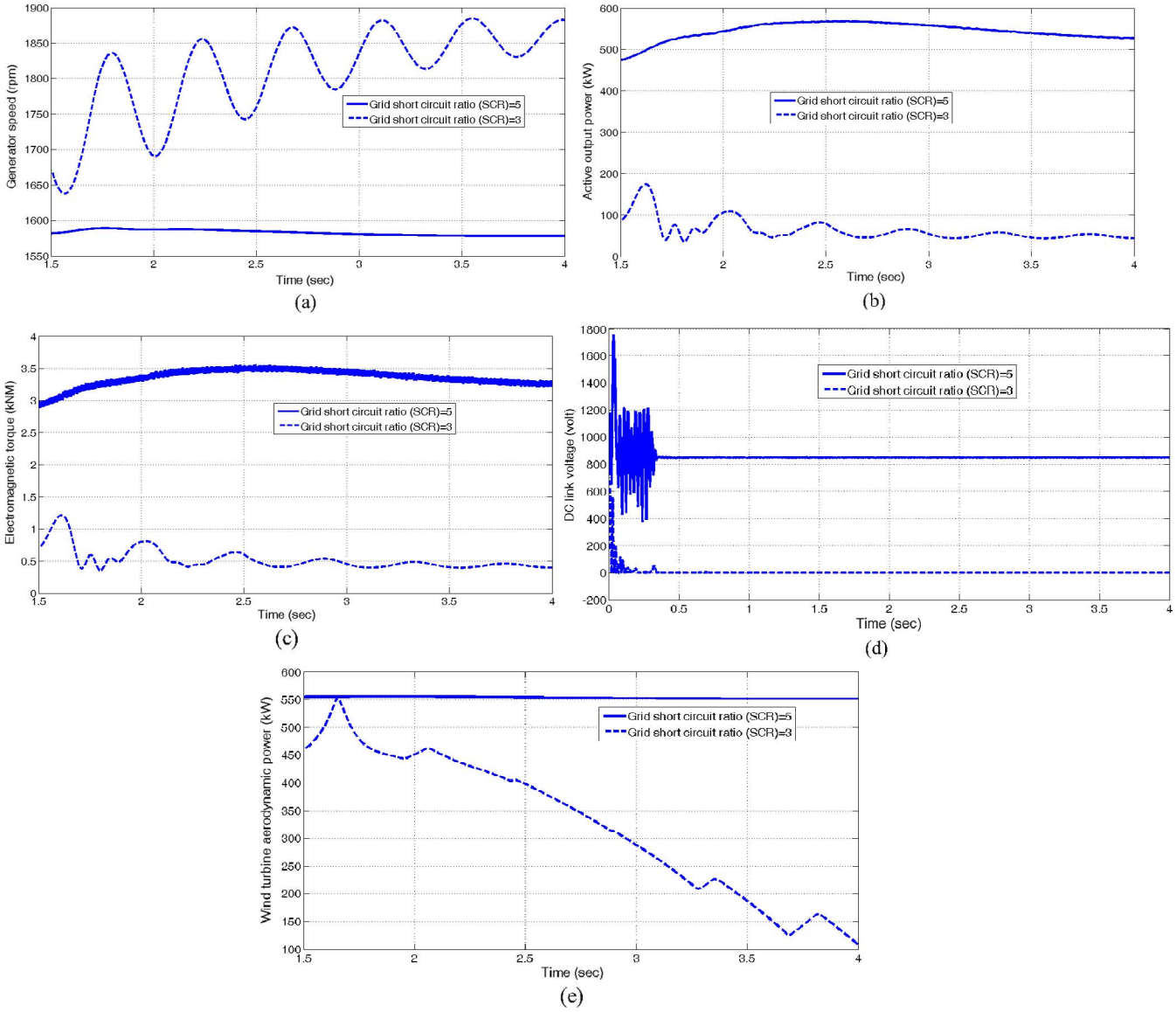

Fig. 16. Study system responses for two different values of grid SCR, (a) generator speed, (b) output active power, (c) electromagnetic torque, (d) DC link voltage, (e) wind turbine aerodynamic power.

From (32), (33) and (10), (11), the stator dynamics in the dq synchronous reference frame can be described as follows:

$$v_s = R_s' i_s + j\omega_s L_s' i_s - j\omega_s \left(s\left(\frac{L_m}{L_r}\right)^2 |L_v| \right) i_s + e_s \tag{34}$$

where $R_s' = R_s + \left(\frac{L_m}{L_r}\right)^2 R_r$ and e_s is the stator induced back emf voltage. Fig. 13(a) depicts the stator dynamic equivalent circuit obtained according to (34), where $L_v' = (s(L_m/L_r)^2 |L_v|)$. From (34), we can also obtain the quasi steady state equivalent circuit of the grid connected DFIG from the stator side point of view, as depicted in Fig. 13(b). The current source i_g in Fig. 13(b) is used for modeling the GSC at quasi steady state conditions.

Considering Fig. 13, the rotor virtual inductance L_v behaves as a negative inductance from the stator side point of view. This in turn, as will be seen, virtually increases the grid SCR and enhances the system stability margin.

According to Fig. 13(b), the linearized dynamics of the rotor current by considering the proposed compensator is given by

$$\frac{L_r'}{\omega_b}\frac{d\Delta i_{rdq}}{dt} = -R_r' \Delta i_{rdq} - \Delta e_{rdq} - j(L_r' - |L_v|) i_{rdq0} \Delta\omega_2 - j(L_r' - |L_v|)\omega_{20} \Delta i_{rdq} + k_{p-i_r}(\Delta i_{rdq-ref} - \Delta i_{rdq}) + \Delta x_{irdq} \tag{35}$$

Table 3 depicts the system modes and corresponding state variables for the case with rotor virtual inductance, and for two different values of grid SCR, i.e. SCR = 3 and 4. Comparing Tables 2 and 3, by implementing the rotor negative virtual inductance, the modes $\lambda_{5,6}$ and thus the whole system will become stable for SCR = 3. Fig. 14 shows the root locus graph of the modes $\lambda_{5,6}$ at SCR = 3, and for gradual change of the $|L_v|$ from 0 to 1 pu. According to Fig. 14, as $|L_v|$ increases, the modes $\lambda_{5,6}$ move toward the left hand side of the s-plane.

6. Simulation results

In this section, at first, performance of the study system of Fig. 4 is examined under two different values of grid short circuit power (SCR), by using time domain simulations. Then, the modified control approach proposed in Section 5 is applied to the rotor side converter, and its capability is examined under weak grid conditions. The system under

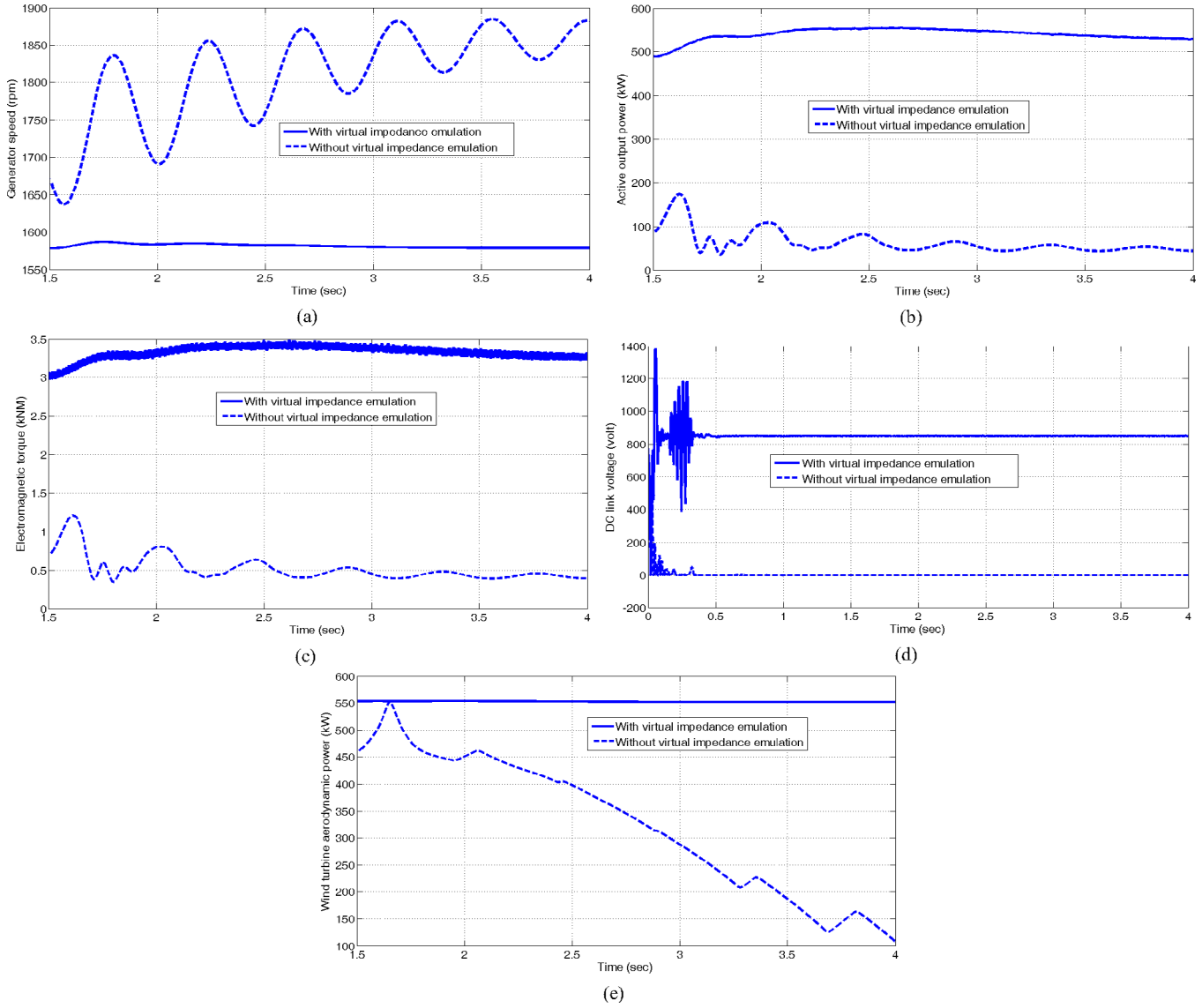

Fig. 17. Study system responses with and without rotor virtual impedance emulation, at grid SCR = 3, (a) generator speed, (b) output active power, (c) electromagnetic torque, (d) DC link voltage, (e) wind turbine aerodynamic power.

study of Fig. 4, is a grid connected 710 kW, 50 Hz DFIG based wind turbine with parameters of Appendix A.

Fig. 15 depicts time responses of the generator speed wr, DFIG output active power Po, electromagnetic torque Te, and WT aerodynamic power (WT captured power) Pt to a step change of wind speed from 10 to 12 m/s, at SCR = 5. In Fig. 15, for SCR = 5 the responses are stable, and before t = 4 s, the wind speed is 10 m/s, wr = 1570 rpm, Po = 430 kW, Te = 2.65 kNM, and Pt = 445 kW. After, t = 4 s, the wind speed reaches the value of 12 m/s, and thus the generator speed increases to 1585 rpm, and Po, Te, and Pt reach the following values at steady state: Po = 615 kW, Te = 3.8 kNM, and Pt = 647 kW. Hence, at normal conditions by increasing the generator speed, the wind turbine captured power Pt and consequently the wind turbine output power Po increases.

Figs. 16 and 17 depict the time responses of the generator speed, DFIG output active power, electromagnetic torque, DC link voltage, and WT aerodynamic power at Vw = 11 m/s.

Fig. 16 shows the responses of the DFIG study system for two different values of the grid short circuit ratio (grid SCR), i.e. SCR = 3 and 5. For SCR = 3, the grid impedance is higher than the one at SCR = 5, and thus the grid has more strength at SCR = 5. According to Fig. 16, the system responses at SCR = 5 are stable, and steady state values of the generator speed wr, output active Po, electromagnetic torque Te, DC link voltage VDC, and WT aerodynamic power Pt, are as follows: wr = 1580 rpm, Po = 530 kW, Te = 3.3 kNM, Pt = 550 kW, where the difference between the Pt and Po represents the system losses. In Fig. 16 at SCR = 5, there is a balance between the WT aerodynamic power and generator output power, and thus the generator speed is stable and equal to 1580 rpm.

On the other hand, at SCR = 3, the wind turbine transfer power capability considerably decreases, and this in turn reduces the wind turbine output power injected to the grid. This consequently results in very low values for the electromagnetic torque and dc link voltage. Even though, the generator electromagnetic torque Te considerably reduced, however, at initial times, the wind turbine aerodynamic torque Tt is relatively constant, and thus due to imbalance between the Te and Tt, the generator speed continuously increases. Also, according to Fig. 16(e), by the increase in the generator speed at the unstable state, Pt also changes and decreases with a higher time constant in comparison with output active power Po. Hence, under low values of the grid SCR, with significant reduction of the WT transfer power capability, Te, Po, Vdc and Pt reach very low values, and wr increases

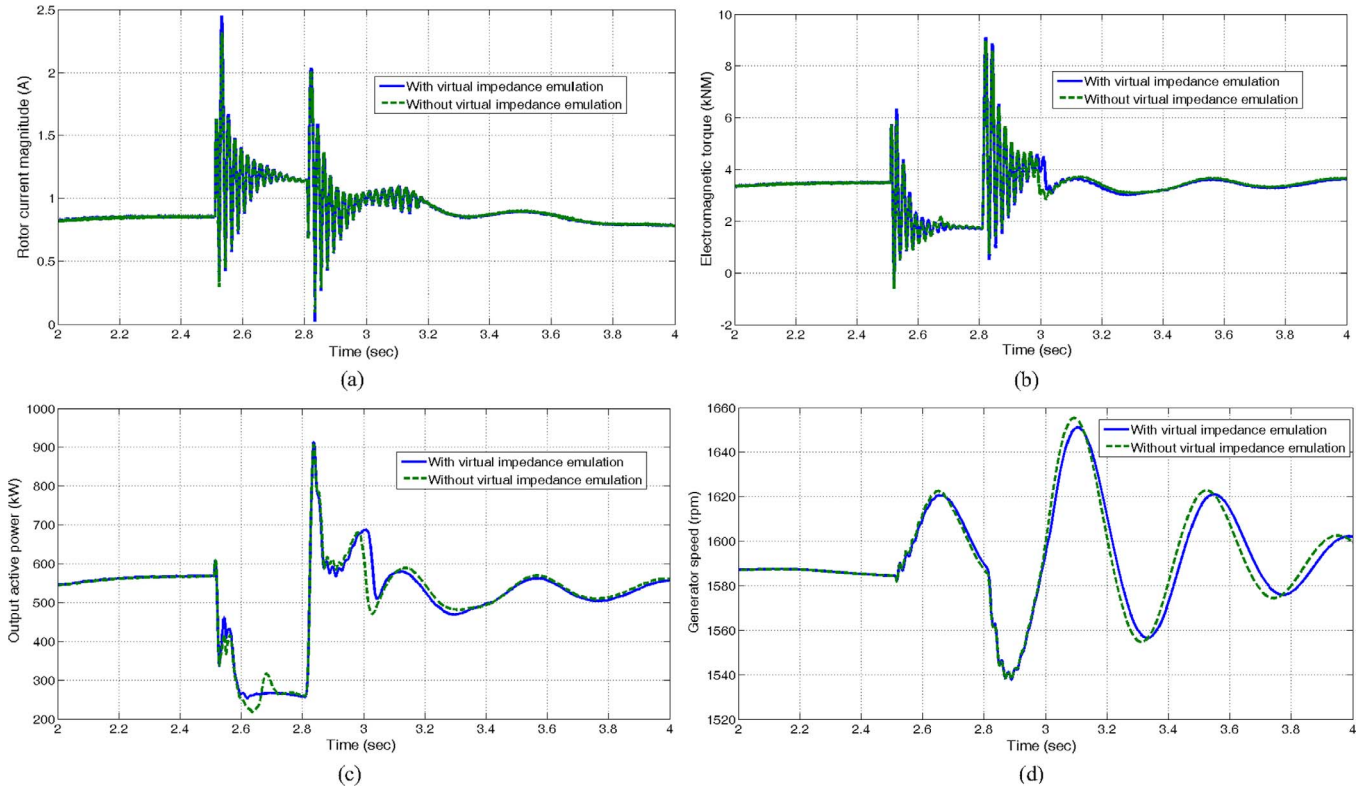

Fig. 18. DFIG time responses with and without rotor virtual inductance emulation, at grid SCR = 5, and under 50% grid voltage dip, (a) rotor current amplitude, (b) electromagnetic torque, (c) output active power, (d) generator speed.

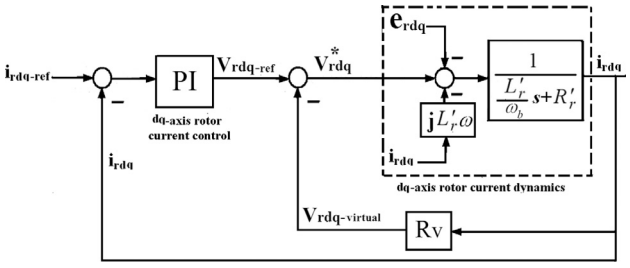

Fig. 19. Modified RSC current control to create the positive virtual resistance.

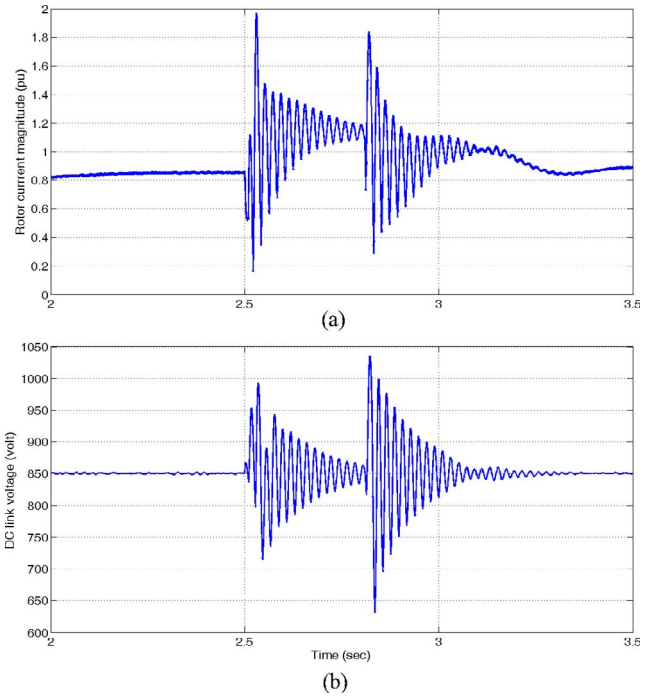

Fig. 20. DFIG time responses with rotor virtual resistance under 50% grid voltage dip, (a) rotor current amplitude, (b) DC link voltage.

continuously, and thus the system becomes unstable. According to Fig. 16, for SCR = 3 and at t = 4 s, the values of the generator speed, output active power, electromagnetic torque, and WT aerodynamic power are as follows: wr = 1885 rpm, Po = 40 kW, Te = 0.42 kNM, and Pt = 107 kW. It is noted that at the modal analysis of Table 2, the DFIG system is stable at SCR = 5, and becomes unstable at SCR = 3. Hence, the simulation results of Fig. 16 are in agreement with the modal analysis results of Table 2.

As stated in Section 5, by modifying the RSC control system, a negative virtual inductance is realized at the rotor side. In Fig. 17, the effectiveness of the modified control approach is studied, at SCR = 3. Fig. 17 depicts the time responses of DFIG system, at SCR = 3, with and without the negative virtual inductance emulation. According to Fig. 17, in the case with the negative virtual inductance emulation, the system responses become stable. This is because, the modified control approach virtually increases the grid SCR and enhances the system stability margin. The time responses of Fig. 17 confirm the modal analysis of Tables 2 and 3, in which the modes $\lambda_{5,6}$ are unstable at SCR = 3, and become stable when the control system is modified to realize the negative virtual inductance.

Fig. 18 shows the impact of the rotor negative virtual inductance on the DFIG low voltage ride through (LVRT) capability. Fig. 18 depicts the time responses of the DFIG system at SCR = 5, and under 50% symmetrical voltage dip, initiated at t = 2.5 s with duration of 300 ms. In Fig. 18, time responses of the rotor current amplitude, electromagnetic torque, output active power, and generator speed are shown, and low voltage ride trough (LVRT) capability of the DFIG system is studied with and without the rotor virtual impedance. It is clear that the

system responses at SCR = 5, with and without the virtual impedance are stable. According to Fig. 18, during the voltage dip, transients appear on the DFIG responses, and at the times of occurring and clearing the fault, the rotor current and DC link voltage increase abruptly. Considering Fig. 18, the DFIG responses with and without the virtual inductance emulation are relatively similar, and thus the proposed compensator does not have significant impact on the LVRT capability of the DFIG system.

In order to enhance the LVRT capability of the system the rotor current control system can be modified to create a positive virtual resistance in series with the rotor. The created virtual resistance limits the rotor current and dc link voltage during moderate voltage dips without activating the crowbar and other protection hardware.

Fig. 19 depicts the modified rotor current control system to create the virtual resistance under transient conditions. In Fig. 19, the feedback gain Rv acts such a resistance Rv in series with the rotor that limits the rotor current under transient conditions. Fig. 20 depicts the rotor current and dc link voltage under 50% voltage dip at t = 2.5 s. According to Fig. 20, it is clear that by using the proposed virtual resistance, the rotor current and dc link voltage are limited below 2 pu, and 1050 V, respectively.

7. Conclusion

This paper deals with the stability analysis and dynamic stability enhancement of the grid connected DFIG based WTs under weak ac grid conditions. Hence, unified dynamic modeling of the whole DFIG system, including the dynamics of the PLL, stator flux, rotor current, drive train, dc-link, RSC and GSC current controllers, dc-link voltage and generator speed controllers, and grid is presented. Then, small signal stability of the full system is carried out and impact of the grid SCR on the stability of the system is examined. It is shown that for the SCR values lower than 3, the modes corresponding to the dc-link voltage and thus the whole system become unstable. Next, the RSC control structure is modified, in which a negative virtual inductance is introduced at the stator side, and thus the grid SCR is virtually increased that stabilizes the system at weak grid connections. Simulation results verify the theoretical analyses and depict that at SCR = 3 and in the case without the virtual impedance emulation, the responses of the electromagnetic torque, output active power and dc-link voltage are unstable and reach very low values. On the other hand, in the case with the negative virtual inductance emulation, the system responses become stable. This is because the modified control approach virtually increases the grid strength and consequently enhances the DFIG stability margin and power transfer capability.

Appendix A. Parameters of a 710 Kw, 690 V, 50 Hz, DFIG-WT

$V_{base} = 690\,\text{V}$ $S_{base} = 710\,\text{KVA}$ $f_{base} = 50\,\text{Hz}$ $\omega_s = 1\,\text{pu}$
$\omega_b = 2\pi f_b = 314\,\text{rad/sec}$ $R_s = 0.008\,\text{pu}$ $R_r = 0.005\,\text{pu}$
$L_s = 3.07\,\text{pu}$ $L_r = 3.056\,\text{pu}$ $L_m = 2.9\,\text{pu}$ $H_g = 0.55\,\text{sec}$
$H_t = 3.5\,\text{sec}$ $k_s = 0.6\,\text{p. u. /elec. rad}$ $D_{tg} = 1.0\,\text{pu}$

Appendix B. Participation factors

To determine the relation between the states variables and modes, the participation factor obtained by (A.1) can be used.

$$p_{ki} = \frac{|\Phi_{ki}||\psi_{ik}|}{\sum_{k=1}^{n} |\Phi_{ki}||\psi_{ik}|} \tag{A.1}$$

where n is the number of state variables, p_{ki} is the participation factor of the kth state variable into mode i, Φ_{ki} is the kth element of the ith right eigenvector of A, ψ_{ki} is the kth element of the ith left eigenvector of A [35].

References

[1] Etxegarai A, Eguia P, Torres E, Fernandez E. Impact of wind power in isolated power system. Electrotech Conf (MELECON). 2012. p. 63–6.
[2] Xi X, Geng H, Yang G. Modelling of the DFIG based wind farms for small signal stability analysis of weak power. 2nd Renew Power Gen Conf (RPG 2013). 2013.
[3] Rahimi M. Coordinated control of rotor and grid sides converters in DFIG based wind turbines for providing optimal reactive power support and voltage regulation. Sustain Energy Technol Assessments-Elsevier 2017;20:47–57.
[4] Rahimi M, Parniani M. Dynamic behavior analysis of doubly-fed induction generator wind turbines – The influence of rotor and speed controller parameters. Electr Power Energy Syst 2010;32:464–77.
[5] Durrant M, Werner H, Abbott K. Model of a VSC-HVDC terminal attached to a weak AC system. Proc of 2003 IEEE conf on control app, CCA 2003, vol. 1. 2003. p. 178–82.
[6] Zhang L. Modeling and control of VSC-HVDC links connected to weak AC systems PhD. Dissertation Stockholm, Sweden: Royal Institute of Technology; 2010.
[7] Zhou Pian, Yuan Xiaoming, Hu Jiabing. Stability of DC-link voltage as affected by phase locked loop in VSC when attached to weak grid. Proc of IEEE PES General Meeting. 2014.
[8] Huang Yunhui, Yuan Xiaoming, Hu Jiabing. Effect of reactive power control on stability of DC-Link voltage control in VSC connected to weak grid. Proc 2014 IEEE PES General Meeting. 2014.
[9] Diedrichs V, Beekmann A, Busker K, Nikolai S, Adloff S. Control of wind power plants utilizing voltage source converter in high impedance grids. Proc IEEE Power Energy Soc (PES) Gen Meeting, San Diego, CA, USA. 2012. p. 1–9.
[10] Diedrichs V, Beekmann A, Adloff S. Loss of (angle) stability of wind power plants-the underestimated phenomenon in case of very low short circuit ratio. Proc 10th Int Workshop Large-Scale Integr Wind Power Power Syst Transmiss Netw OffshoreWind Power Plants, Aarhus, Denmark, Oct. 25–26. 2011. 393–340.
[11] Zhou JZ, Ding H, Fan S, Zhang Y. Impact of short-circuit ratio and phase-locked-loop parameters on the small-signal behavior of a VSC HVDC converter. IEEE Trans Power Del 2014;29(5):2287–96.
[12] Huang Y, Yuan X, Hu J, Zhou P. Modeling of VSC connected to weak grid for stability analysis of DC-link voltage control. IEEE J Emerg Selected Topics Power Elec 2015;3(4):1193–204.
[13] Hu J, Hu Q, Wang B, Tang H, Chi Y. Small signal instability of PLL-synchronized type-4 wind turbines connected to high-impedance AC grid during LVRT. IEEE Trans Energy Convers 2016;31(4):1676–87.
[14] Rahimi M. Dynamic performance assessment of DFIG-based wind turbines: A review. Renew Sustain Energy Rev 2014;37:852–66.
[15] Wu F, Zhang XP, Godfrey K, Ju P. Small signal stability analysis and optimal control of a wind turbine with doubly fed induction generator. IET Gen Transm Distrib 2007;1:751–60.
[16] Wu F, Zhang XP, Godfrey K K, Ju P. Modeling and control of wind turbine with doubly fed induction generator. Proc IEEE PSCE Conf. 2006. p. 1404–9.
[17] Mei F, Pal B. Modal analysis of grid-connected doubly fed induction generators. IEEE Trans Energy Convers 2007;22:728–36.
[18] Yang B, Jiang L, Wang L, Yao W, Wu QH. Nonlinear maximum power point tracking control and modal analysis of DFIG based wind turbine. Electr Power Energy Syst 2016;74:429–36.
[19] Liu J, Meng H, Hu Y, Lin Z, Wang W. A novel MPPT method for enhancing energy conversion efficiency taking power smoothing into account. Energy Convers Manage 2015;101:738–48.
[20] Wang D, Hu J, Huang Y, Wang N, Zhou Q. Stability of DC-link voltage affected by phase-locked loop for DFIG based wind turbine connected to a weak AC system. 17th int conf elec machines and systems (ICEMS). 2014.
[21] Wang Z, Shen C, Liu F. Impact of DFIG with phase locked loop dynamics on power systems small signal stability. IEEE Power Energy Society Gen. Meeting; 2014.

[22] Hu J, Huang Y, Wang D, Yuan H, Yuan X. Modeling of grid-connected DFIG-based wind turbines for DC-link voltage stability analysis. IEEE Trans Sustain Energy 2015;6(4):1325–36.
[23] Xiang D, Ran L, Tavner PJ, Yang S. Control of a doubly fed induction generator in a wind turbine during grid fault ridethrough. IEEE Trans Energy Convers 2006;21(3):652–62.
[24] Lima FKA, Luna A, Rodriguez P, Watanable EH, Blaabjerg F. Rotor voltage dynamics in the doubly-fed induction generator during grid faults. IEEE Trans Power Electron 2009;25(1):118–30.
[25] Mukhopadhyay B, Mandal RK. Voltage compensation using PSO-PI controlled STATCOM in a DFIG-based grid-connected wind energy system. Int Conf Elec Power and Energy Systems (ICEPES). 2016. p. 88–93.
[26] Galal M, Saad MS, Abou El-Zahab EE. Improving voltage stability of wind farms connected to weak grids using FACTS. 16th International Middle-East Power Systems Conf., MEPCON'2014, AinShams University, Cairo, Egypt, December 23–25. 2014.
[27] Kamarposhti MA. A comparative study of the implementation wind farms integration based on maximization of voltage stability and system loadability. Trakia J Sci 2016;3:294–304.
[28] Anzum, Shankar CB, Prakash R. Stability enhancement of DFIG-based wind farm connected to a grid using STATCOM. Annual IEEE India Conf (INDICON). 2015. p. 1–5.
[29] Murthy S, Devki P, Devishree J. A static compensation method based scheme for improvement of power quality in wind generation. Int Conf on Control and Computing (PACC). 2011. p. 2–7.
[30] Sattar A, Al-Durra A, Muyeen SM. Real time implementation of STATCOM to analyze transient and dynamic characteristics of wind farm. 37 Annual Conf. IEEE Ind. Elec. Society (IECON2011). 2011.
[31] Blaabjerg F, Teodorescu R, Liserre M, Timbus AV. Overview of control and grid synchronization for distributed power generation systems. IEEE Trans. Indus. Electron. 2006;53(5):1398–409.
[32] Golestan S, Monfared M, Freijedo FD, Guerrero JM. Performance improvement of a prefiltered synchronous-reference-frame PLL by using a PID-type loop filter. IEEE Trans Ind Elec 2014;61(7).
[33] Rahimi M, Parniani M. Efficient control scheme of wind turbines with doubly-fed induction generators for low voltage ride-through capability enhancement. IET Renew Power Gener 2010;4(3):242–52.
[34] Rahimi M. Drive train dynamics assessment and speed controller design in variable speed wind turbines. Renew Energy-Elsevier 2016;89:716–29.
[35] Kundur P. Power system stability and control. 1st ed. USA: McGraw-Hill; 1994.